

Characterization of High-Purity Germanium Detectors with Amorphous Germanium Contacts in Cryogenic Liquids

R. Panth¹, J. Liu^{1,b}, I. Abt², X. Liu², O. Schulz², W.-Z. Wei¹, H. Mei¹,
D.-M. Mei¹, G.-J. Wang¹

¹University of South Dakota, 414 East Clark Street, Vermillion, SD 57069, USA

²Max-Planck-Institut für Physik, Föhringer Ring 6, D-80805 München, Germany

Received: date / Accepted: date

Abstract For the first time, planar high-purity germanium detectors with thin amorphous germanium contacts were successfully operated directly in liquid nitrogen and liquid argon in a cryostat at the Max-Planck-Institut für Physik in Munich. The detectors were fabricated at the Lawrence Berkeley National Laboratory and the University of South Dakota, using crystals grown at the University of South Dakota. They survived long-distance transportation and multiple thermal cycles in both cryogenic liquids and showed reasonable leakage currents and spectroscopic performance. Also discussed are the pros and cons of using thin amorphous semiconductor materials as an alternative contact technology in large-scale germanium experiments searching for physics beyond the Standard Model.

Keywords HPGe · Amorphous germanium · Liquid nitrogen · Liquid argon

1 Introduction

If the decay of heavy Majorana neutrinos [1–4] in the early universe into leptons and antileptons created a slight matter and antimatter asymmetry [5, 6], the observed asymmetry in our current universe can be explained with the help of Leptogenesis [7, 8], which is a theory that converts the lepton-antilepton asymmetry to a baryon-antibaryon asymmetry. The existence of heavy Majorana neutrinos is predicted by the seesaw mechanism [9–11] to explain the tiny masses of the observed neutrinos compared to other leptons, such as

electrons. Light neutrinos must also be of Majorana type in the scenario of the seesaw mechanism. In this case, neutrinos are their own antiparticles, and neutrinoless double-beta ($0\nu\beta\beta$) decay [12, 13] becomes possible.

In GERDA [14, 15], an experiment searching for the $0\nu\beta\beta$ decay of ^{76}Ge , and the follow-up experiment LEGEND [16], a merger of GERDA and MJD [14, 17], high-purity germanium (HPGe) detectors are operated directly in liquid argon (LAr), which acts as a coolant, a passive radioactive background shielding, and an active background veto. The detectors deployed are mostly *p*-type point-contact (PPC) HPGe detectors [18, 19] and broad-energy germanium (BEGe) detectors [20, 21] with most their surfaces being lithium-diffused contact layer as shown in Fig. 1 left. The layer is typically 1 mm thick, reducing the active volume substantially, especially when the transient region underneath the lithium-diffused layer is taken into account. To illustrate, consider a small PPC detector with a diameter of 3 cm and a height of 3 cm, the lithium-diffused layer and the transient layer beneath it may take up to 26% of the overall volume. The number drops to about 9% for a detector with a diameter of 8.4 cm and a height of 10 cm, which is still a non-negligible fraction considering the price of a ^{76}Ge -enriched PPC.

An additional consideration are background events mimicking $0\nu\beta\beta$, induced by electrons from beta decays on the surface of the detector. An example of these are ^{42}K (daughter of ^{42}Ar) decays with a Q-value of 3525 keV, which can be recorded with an energy in the region of interest around 2039 keV (Q-value of $0\nu\beta\beta$ of ^{76}Ge) due to partial charge collection in the outer layers of the detector. An artificial enlargement of the lithium-diffused layer has been discussed but that would lead to a further loss in active volume.

^aThis work was supported by NSF OISE-1743790, PHYS-1902577, OIA-1738695, DOE FG02-10ER46709, the Office of Research at the University of South Dakota and a research center supported by the State of South Dakota.

^bCorresponding author E-mail address: jing.liu@usd.edu

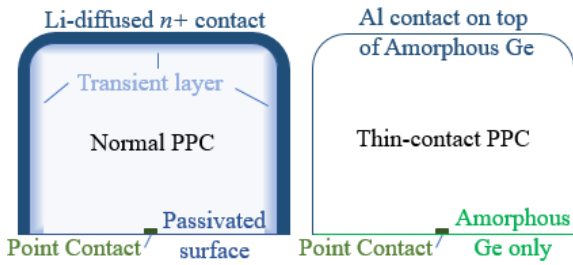


Figure 1 Comparison between a normal and a thin-contact PPC HPGe detector (not to scale).

An attractive alternative are thin contacts as shown in Fig. 1 right. There are already commercial PPC detectors with their end surfaces made of thin contacts that are sensitive to α , β , and low energy X -rays [22]. Should the entire lithium-diffused contact be replaced by such a thin one, the sensitive volume of a large PPC can be enlarged by about 9%, which is favorable for the tonne-scale LEGEND experiment.

Since the thin contact is sensitive to α and β particles, such a technique has to be combined with the use of underground argon [23], careful selection of materials close to the detector, avoidance of surface contamination, and an active veto using LAr scintillation light.

Thin contacts can be easily segmented. Signals from a surface segment normally have worse energy resolution than those from the point-contact due to the larger capacitance of the segment. However, they can be used to precisely determine the start time of an event in a PPC, especially of an event close to the surface. Combining the time information from segments and the energy information from the point-contact, better identification of surface events becomes possible.

More contacts call for more readout cables and front-end electronics, which may bring in more background. Once the number of segments becomes too large, the background induced may cancel out the benefits. Detailed Monte Carlo studies are needed to figure out an optimized segmentation scheme. A simple scheme for a PPC detector would be a segment for its side surface and another for the end surface opposite to the point-contact side.

A mature technique to make thin contacts is to sputter germanium or silicon on bare HPGe crystals followed by the deposition of a thin layer of aluminum to form electrodes [24–27]. The sputtered germanium forms an amorphous germanium layer, which is about a few hundred nanometre thick. It can block the injection of both electrons and holes from contacts to the bulk of a detector, while allows charge carriers from the bulk to be collected on contacts [28]. In the surface area not covered by aluminum electrodes, it works

as a passivation layer to protect the crystalline HPGe inside.

The technique has been used to produce large planar strip HPGe detectors by Mark Amman at the Lawrence Berkeley National Laboratory (LBNL) [29] to detect X -rays in the COSI [30, 31] experiment. The properties of thin contacts have been thoroughly examined [31] and has survived very harsh operating environments, including a crash-landing of a COSI balloon.

A dozen mini planar detectors have been fabricated at the University of South Dakota (USD) using the technique developed at LBNL and HPGe crystals produced at the USD crystal pulling facility [32]. They perform well in a traditional vacuum cryostat [33]. A cryostat, Gerdalinen II [34], has been developed at the Max-Planck-Institut (MPI) für Physik in Munich to study segmented HPGe detectors directly submerged in cryogenic liquids, including liquid nitrogen (LN_2) and LAr. Reported in this paper is work carried out in summer 2019 to study the feasibility of operating HPGe detectors with thin amorphous germanium surfaces directly in LN_2 and LAr.

2 Experiment

2.1 USD Detectors with Amorphous Germanium Surfaces

Three mini planar HPGe detectors with amorphous germanium surfaces were used in this study. They were made from HPGe crystals grown at USD. Their dimensions and properties are summarized in Table 1.

Cylindrical HPGe crystal boules from Czochralski pullers operated at USD were first diced into about $2 \times 2 \times 1 \text{ cm}^3$ cuboid with diamond wire saws and grinding blades. One of them was sent to LBNL, where the detector USD-8-4-15 was fabricated. The detailed fabrication process of this detector is described elsewhere [29]. At USD, each cuboid was further ground into a top hat shape, as shown in Figs. 2 and 3. The brims were used to handle the crystals so that their sensitive surfaces were kept untouched during fabrication and operation. The top and bottom surfaces of the crystals were lapped using silicon carbide and aluminum oxide with 17.5 and 9.5 micron grids, respectively, to remove visible scratches from cutting. All pieces were then submerged in a mixture of HF and HNO_3 acids to etch away small surface defects. After rinsed in de-ionized water and dried with nitrogen gas, all surfaces were shiny and reflective.

Amorphous germanium was deposited on all surfaces in a radio-frequency sputtering machine. The sputtering was done in a 93:7 mixture of Ar and H_2 gas at

Table 1 Summary of USD detector properties.

Detector	USD-RL	†USD-8-4-15	USD-R02
Impurity/cm ³	6.2×10^9	1.7×10^{10}	2.9×10^{10}
Thickness/cm	1.07	0.70	0.65
Top area/cm ²	1.88×1.79	1.27×1.20	$\ddagger 0.5 \times 0.5$
* V_d/V	400	400	700
◊ I_{before}/pA	10	1	‡1
◊ I_{LN_2}/pA	5	0	‡1
◊ I_{LAr}/pA	210	10	‡25
◊ I_{after}/pA	7	-	‡42
• $\Delta E_{\text{puls}}^{\text{before}}/keV$	1.93	1.28	1.67
• $\Delta E_{\text{puls}}^{\text{before}}/keV$	2.55	1.66	2.16
• $\Delta E_{\text{puls}}^{LN_2}/keV$	5.63	5.64	-
• $\Delta E_{\text{puls}}^{LN_2}/keV$	5.92	5.81	-
• $\Delta E_{\text{puls}}^{LAr}/keV$	5.44	-	5.42
• $\Delta E_{\text{puls}}^{LAr}/keV$	5.91	-	6.01
• $\Delta E_{\text{puls}}^{\text{after}}/keV$	1.10	-	1.10
• $\Delta E_{\text{puls}}^{\text{after}}/keV$	1.74	-	3.22

† Made by Mark Amman at LBNL in 2015.

‡ Values are for the central contact.

* V_d : Depletion voltage.

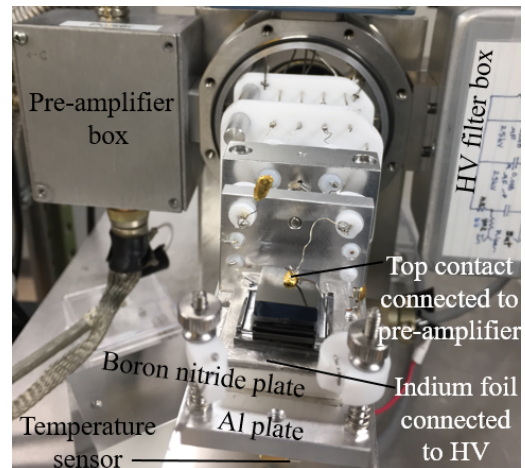
◊ I : leakage current measured at 1200 V in LN₂, LAr, and vacuum before/after the MPI deployment

• ΔE : energy resolutions of the pulser and the 662 keV γ -ray peak measured at 1200 V in LN₂, LAr and vacuum before/after the MPI deployment.

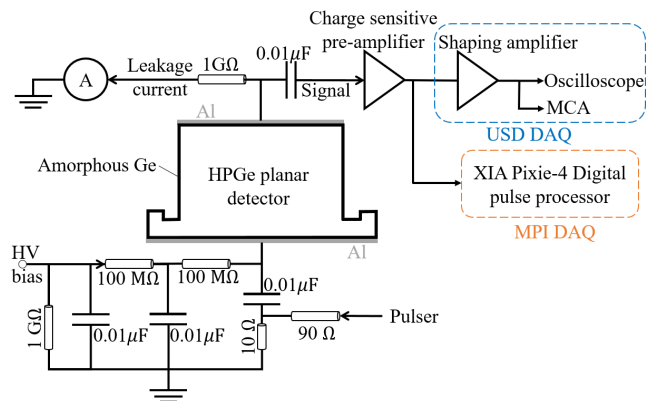
14 mTorr. The duration of the sputtering was carefully controlled such that the thickness of the amorphous germanium layers became about 300 nm. Aluminum contacts were then evaporated on the top and bottom surfaces using an electron-beam evaporator for the detectors USD-R02 and USD-8-4-15. For the detector USD-RL, the aluminum contacts were sputtered on. Any undesired deposition of aluminum on the side surfaces was etched away in a 1% HF solution. The final contact structure is sketched in Fig. 3. The fabrication procedure at USD was almost identical to the one used at LBNL [32], with only minor adjustments to accommodate for different devices.

2.2 Detector Characterization in Vacuum

Prior to the deployment of the detectors at MPI, their leakage currents, depletion voltages, and energy resolutions were measured in a vacuum cryostat at USD. Its internal structure is shown in Fig. 2. The aluminum stage where the detectors were placed was cooled by a stainless steel tube filled with LN₂. A temperature sensor was placed at the bottom of the stage. The lowest operation temperature of the stage was measured to be 78 K. All the measurements were done one hour after the stage reached 78 K to allow the detector to be in equilibrium with the stage.

**Figure 2** Internal structure of the vacuum cryostat at USD.

A schematic of the electronic circuit is shown in Fig. 3. The detector was biased through its bottom contact, and read out at the top contact. Being a direct current, the leakage current, I , could not pass the $0.01 \mu\text{F}$ capacitor before the charge sensitive pre-amplifier, but the $1 \text{ G}\Omega$ resistor before the ammeter, and was measured there. Transient signals, however, could not pass the resistor, but the capacitor, and were amplified thereafter. The ammeter used in the MPI setup was a Keithley picoammeter, which can measure leakage currents down to 20 fA. The instrument used at USD was a combination of a transimpedance amplifier and a regular multimeter, the precision of which was only 1 pA. The leakage currents of the detectors in different environments at 1200 V are summarized in Table 1.

**Figure 3** Electronic circuit for detector characterization.

Leakage currents in these mini planar HPGe detectors arise mainly due to charge injections at their top and bottom contacts (bulk leakage) and the leakage through defects on the side surfaces (surface leakage). The two types of leakages could be measured separately in one

case as a ring of aluminum was etched away from the top contact, which was separated into a small central contact and a surrounding guard contact consequently. The leakage current measured from the central contact was mainly due to charge injections. The one measured from the guard contact was mainly due to the side surface leakage. Detector USD-R02 was used for such measurements before being repurposed for this study, hence it had two contacts on its top surface as shown in Fig. 10. Without such a structure, the measured leakage currents of the other two detectors were a sum of the bulk and the surface leakages.

The amount of leakage current is an important indicator for the quality of the contacts and side passivation of a detector. It increases with the bias voltage and the temperature, as predicted by the model developed by Döhler, Brodsky and Schottky and successfully applied to amorphous germanium contacts on HPGe detectors [35]. It may also change over the first few thermal cycles after fabrication and gradually stabilizes afterward [36]. A detailed study of the leakage currents of the USD detectors can be found in Ref. [37]. On average, the bulk leakage is around a few pA, the surface leakage is around a few tens of pA, at 78 K. In contrast, detectors made at LBNL using USD crystals typically have a combined leakage below 1 pA.

To avoid charge trapping due to low electric field in some part of a detector, the operation voltage should normally be much higher than the depletion voltage. It is hence of interest to measure the latter to help determine the former. In addition, the depletion voltage of a planar detector, V_d , is associated with the net impurity concentration of the HPGe crystal through the following equation:

$$|N_A - N_D| = 2\varepsilon V_d / e / D^2,$$

where N_A and N_D are the p and n -type impurity concentrations, respectively, ε is the permittivity of Ge, e is the elementary charge, and D is the detector thickness. The measurement of V_d can then be used to verify the net impurity level given by the Hall-effect measurement of the crystal.

A scan of the detector capacitance, C_d , at various bias voltages, V_b , can be used to determine V_d . This can be understood as follows. As the bias voltage of the detector, V_b , goes up, the thickness of the depleted region, d , increases, the detector capacitance, C_d , goes down, because C_d is anti-proportional to d . When the detector is fully depleted, $d = D$, and cannot increase any more, C_d becomes a constant thereafter. The bias voltage at the point where the C_d - V_b curve starts to flatten out is therefore the depletion voltage, V_d .

C_d was not measured directly, its bias voltage dependence was estimated as follows:

- Inject step voltage pulses with a fixed amplitude, V_p , from a pulser to the circuit.
- The voltage change is converted to charge injection to the detector through the $0.01 \mu\text{F}$ capacitor in between the pulser and the detector.
- This change of charges can be converted to a voltage pulse, V_o , by the charge-sensitive pre-amplifier.
- Given a fixed charge injection, q , the output voltage, V_o , is proportional to C_d , according to the relation $q = CV$ that applies to an ideal planar capacitor.

The V_o - V_b curve hence has the same behavior as the C_d - V_b curve. Thus, the full depletion voltage can be determined using the former. Figure 4 shows the V_o - V_b (relative capacitance versus bias) curves for the three detectors. Their bias voltages are marked in the figure and summarized in Table 1.

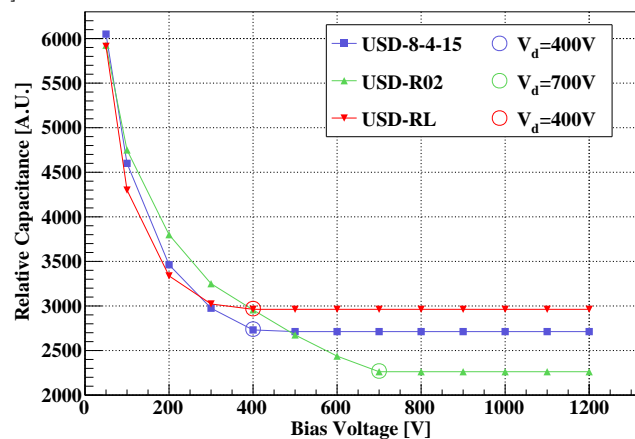


Figure 4 Relative capacitance as a function of bias voltage.

The energy resolution of an HPGe detector is a convolution of three major components, the electronic noise ΔE_e , the fluctuation of the number of charge carriers in their creation process ΔE_n , and a component due to trapping of charge carriers ΔE_t :

$$\Delta E^2 = \Delta E_e^2 + \Delta E_n^2 + \Delta E_t^2.$$

Since pulser signals do not originate from physical events, the fluctuation of their pulse heights depends only on the electronic noise. The resolution of the peak in the energy spectrum due to pulse-injection is hence a good indicator of the electronic noise ΔE_e . A γ -ray peak should be wider than the pulser peak due to the additional contributions of ΔE_n and ΔE_t . This is shown clearly in Figure 5, which is the energy spectrum measured for the detector USD-RL biased at 1200 V in the vacuum cryostat at USD. The spectrum was taken with

a ^{137}Cs radioactive source placed outside the cryostat above the detector. Rectangular pulses with a fixed amplitude were used to generate the pulser peak slightly above 1 MeV in the spectrum. The resolution of the pulser peak is $\Delta E_e = 1.10$ keV. The resolution of the 662 keV peak is $\Delta E = 1.74$ keV, which is larger than ΔE_e .

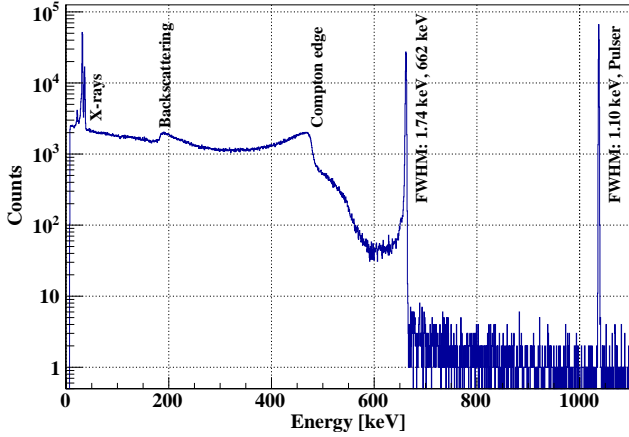


Figure 5 Energy spectrum obtained with the vacuum cryostat at USD, a ^{137}Cs source, and the USD-RL detector after its tests in LN_2 and LAr at MPI.

2.3 Cryostat at MPI

A liquid argon cryostat named Gerdalinen II was developed by the germanium detector group at MPI for the operation of up to three segmented HPGe detectors in cryogenic liquids [34]. An artist view is shown in the left part of Fig. 6. It was used for the operation of USD detectors in LN_2 and LAr. The top flange of Gerdalinen II is opened vertically for installation. Detector holders and the central part of the infrared (IR) shield are attached to a vertical stainless steel bar, which is fixed to the top flange. The assembly is lifted together with the top flange.

For the operation of the USD detectors, a simple PTFE stage was mounted to the lowest position on the vertical bar as shown in Fig. 7. An indium foil was pressed on top of the stage using two PTFE bars. A rigid high voltage (HV) cable went through the vertical PTFE bar and was pushed tightly against the indium foil to provide the bias voltage. The detector was placed on top of the indium foil. A pogo pin connected to the signal cable was pressed lightly on the top surface of the detector. Three PT100 temperature sensors were mounted along the stainless steel bar. The lowest one was slightly below the bottom of the detector. The middle one was a few centimeters above the detector.

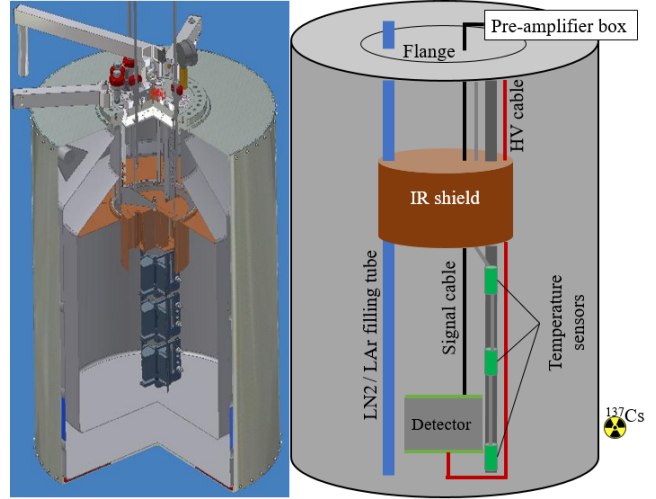


Figure 6 Left: technical drawing of the MPI cryostat. Right: schematics of its internal wiring.

The top one was close to the IR shield. They were used to monitor the liquid level in the cryostat. The internal wiring scheme is shown on the right side of Fig. 6.

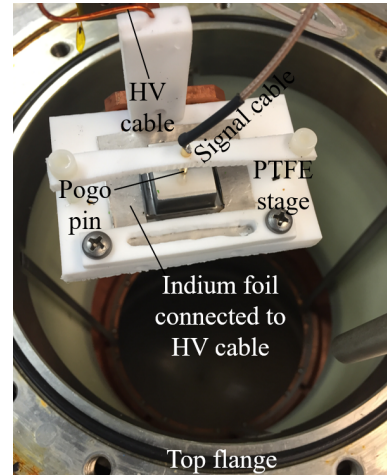


Figure 7 Detector to be lowered into the MPI cryostat.

There were safe procedures to fill and empty Gerdalinen II to avoid any frosting of the detectors.

2.4 Detector Operation in Liquid Nitrogen

The detectors were first operated in LN_2 . The same measurements as those done at USD were repeated in the new environment: the leakage current and the relative capacitance as functions of bias voltage, and the energy resolution of the 662 keV γ -ray peak from a collimated 5 MBq ^{137}Cs source at 1200 V.

Figs. 8, 9 and 11 show the leakage currents of the three detectors as functions of their bias voltages after

each thermal cycle in LN₂. For reference, data sets taken in the vacuum cryostat at USD before and after the MPI deployment were plotted in the same figures.

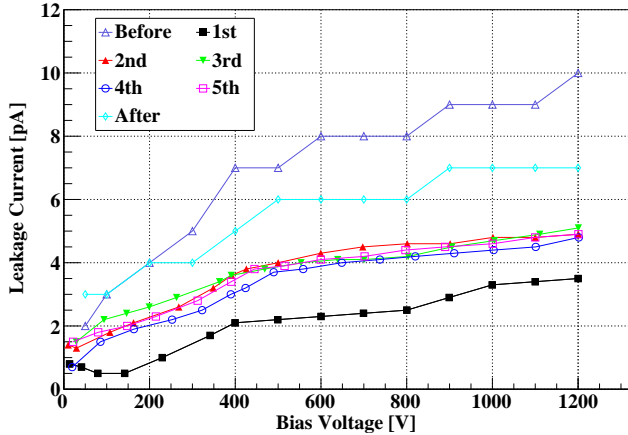


Figure 8 Leakage current of detector USD-RL as a function of its bias voltage in LN₂, except for the “Before” and “After” data sets, which were measured in vacuum at USD before and after the MPI deployment, respectively. The numbers denote thermal cycles in LN₂.

The leakage current of detector USD-RL measured during the first cooling cycle was 3.5 pA at 1200 V, shown as the last point in the lowest curve in Fig. 8. It was monitored thereafter and a slow increase was observed over time. After about an hour, the leakage current stabilized at 5.1 pA. The leakage current after that was very stable over five thermal cycles. A current of 5 pA at 1200 V was always observed. The data sets denoted as “before” and “after” were measured in the vacuum cryostat at USD before and after the MPI deployment. They are slightly higher than those measured in LN₂. This is because the real temperature of the detectors in the vacuum cryostat was a few degrees higher than the LN₂ temperature, and the leakage current increases with temperature. Overall, there was no significant change of the leakage current for detector USD-RL measured in different thermal cycles and environments, and all currents were below 10 pA up to 1200 V.

As shown in Fig. 9, the leakage current of detector USD-8-4-15 was basically around 1 pA in both environments, except for the data set measured during the first cool down, which increases rapidly after 1500 V. One possible explanation is that some dust attached itself to the surface of this detector during the process of moving it from USD to MPI, and created a surface leakage channel, which was washed or blown off from the surface in the first cooling cycle; as the leakage channel was removed, the detector behaved normally afterward.

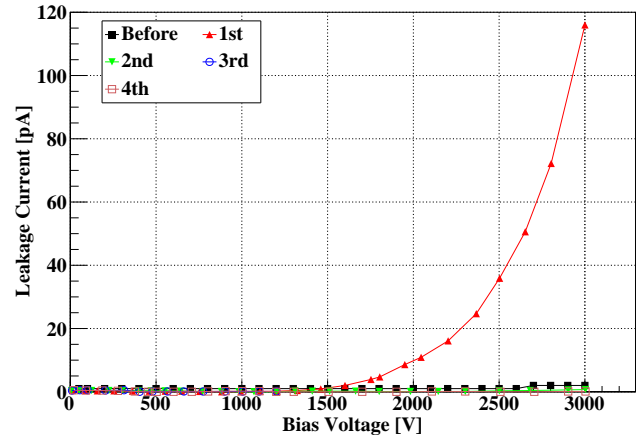


Figure 9 Leakage current of detector USD-8-4-15 as a function of its bias voltage in LN₂, except for the data set denoted as “Before”, which was measured in vacuum at USD before the deployment at MPI. The numbers denote thermal cycles in LN₂.

Only one read-out channel could be used in the MPI cryostat. The central and the guard contacts on the top surface of detector USD-R02 were connected to it through a pogo pin one at a time, the other contact was left floating as shown in Fig. 10. In contrast, both contacts were read out in the vacuum cryostat at USD.

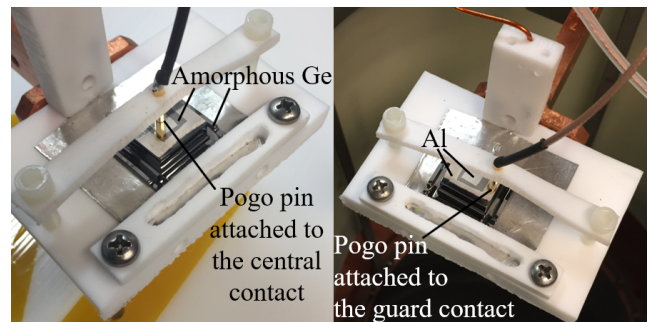


Figure 10 Two different contact schemes of the guard-ring detector USD-R02 in the MPI cryostat.

As shown in Fig. 11, the leakage currents of USD-R02 in different contacts, environments and thermal cycles were mostly below 5 pA, except for the bulk leakage measured at USD after the MPI deployment, which may be due to a damage to the detector surface during the shipment as a small scratch was observed on its top surface.

The “capacitance” versus bias voltage curves measured in LN₂ were basically identical to those measured in vacuum. The depletion voltages determined this way were the same as those determined at USD. This was as expected since the depletion voltage is basically determined by the impurity level of the crystal and should not change with the environment at a given temperature.

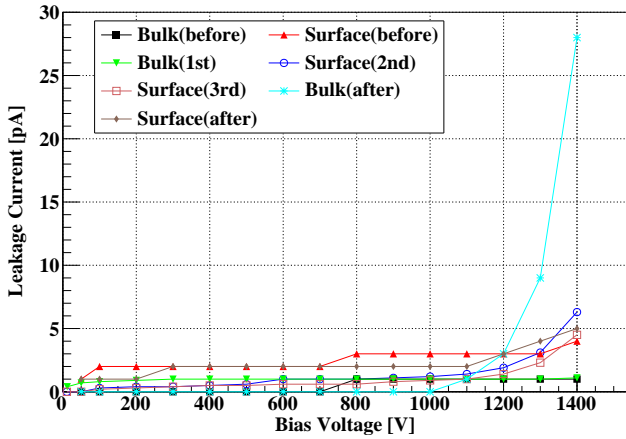


Figure 11 Leakage currents of detector USD-R02 versus its bias voltage in LN₂, except for the data sets marked with “before” and “after”, which were measured in the vacuum cryostat at USD before and after the MPI deployment. The bulk leakage currents were measured through the central contact. The surface leakage currents were measured through the guard contact.

The energy spectrum of ¹³⁷Cs taken with detector USD-RL in LN₂ is shown in Fig. 12. The right most peak was generated by injecting to the detector voltage pulses with a fixed amplitude. The FWHM of this peak was 5.63 keV, indicating large electronic noise. There was no effort made to optimize the read-out as it was beyond the goal of this study. A standard way to improve this is to move the front-end jFET from the pre-amplifier board to somewhere inside the cryostat, a few centimeters above the liquid level, to reduce the signal cable length and to achieve an optimized operating temperature of the jFET. Nevertheless, the spectrum measured in LN₂ was very similar to that measured in vacuum (Fig. 5).

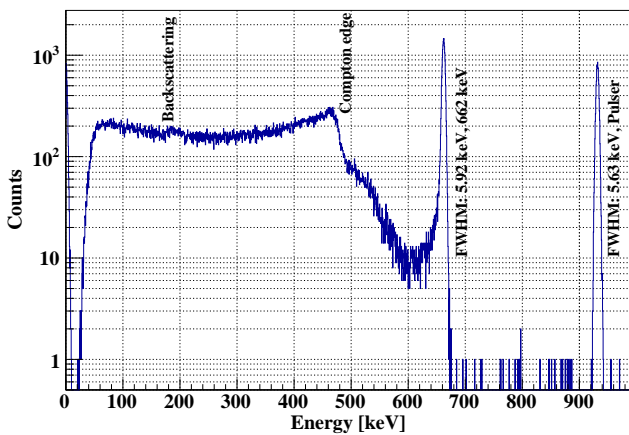


Figure 12 Energy spectrum of ¹³⁷Cs taken with detector USD-RL in LN₂.

2.5 Detector Operation in Liquid Argon

The same measurements were repeated with the same detectors in LAr using the same cryostat at the MPI. Figs. 13, 14 and 15 show the leakage currents of the three detectors as functions of their bias voltages after each thermal cycle in LAr. For reference, data sets taken in the vacuum cryostat at USD before and after the MPI deployment were plotted in the same figures, and labeled as “before” and “after”, respectively.

Detector USD-RL went through two more thermal cycles in LAr. The leakage currents were about 20 times higher than those measured in LN₂.

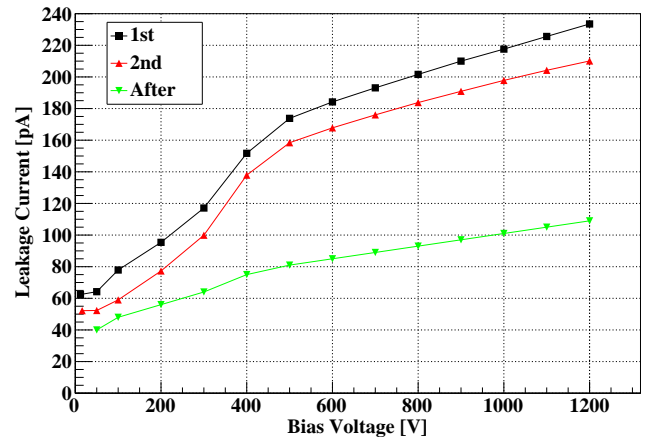


Figure 13 Leakage currents of detector USD-RL versus its bias voltage in LAr, except for the data set labeled “after”, which was measured in the vacuum cryostat at USD after its deployment at MPI. The numbers denote individual thermal cycles in LAr.

Detector USD-8-4-15 was operated in LAr once. Below 800 V, the leakage current was below 1 pA. Its significantly lower leakage current is a clear evidence that the quality of the amorphous germanium surface made at LBNL was better than that made at USD. The quick rise of the leakage current above 800 V was due to damage to the detector when it fell from the PTFE stage during the preparation of the fifth thermal cycle in LN₂. Nonetheless, it still had the best performance compared to the other two detectors.

USD-R02 was operated twice in LAr, the first time with its central contact connected to the signal cable, the second time with its guard contact connected to the signal cable. The bulk leakage increased a few times compared to those in LN₂, the surface leakage increased about 20 times. Note, that the leakage current of detector USD-RL in LAr was also increased by about 20 times, which was probably also dominated by surface leakage.

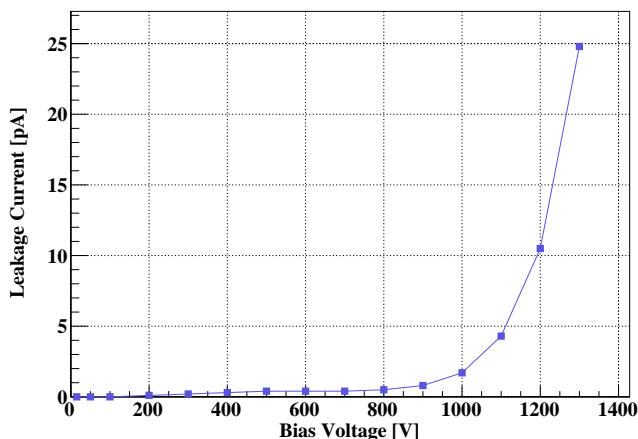


Figure 14 Leakage current of detector USD-8-4-15 versus its bias voltage in LAr.

The measurements at USD after the MPI deployment were done at about 90 K instead of 78 K to be closer to the LAr temperature.

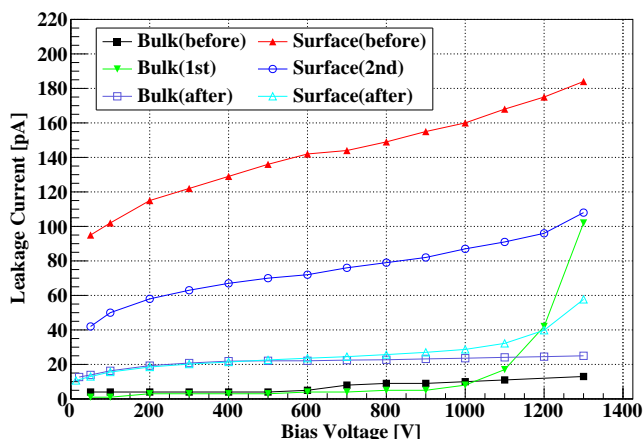


Figure 15 Leakage currents of detector USD-R02 versus its bias voltages in LAr, except for the ones labeled “before” and “after”, which were measured in the USD vacuum cryostat at 90 K. The numbers denote the thermal cycles in LAr. All thermal cycle measurements were carried out at LAr temperature at MPI. The bulk leakage currents were measured through the central contact. The surface leakage currents were measured through the guard contact.

The energy spectrum of ^{137}Cs measured with detector USD-RL biased at 1200 V in LAr is shown in Fig. 16. The energy resolution and the noise level were similar to those measured in LN_2 .

2.6 Characterization in Vacuum Again

Detectors USD-RL and USD-R02 were characterized in vacuum after the operation in cryogenic liquids, which confirmed that the detectors could still function nor-

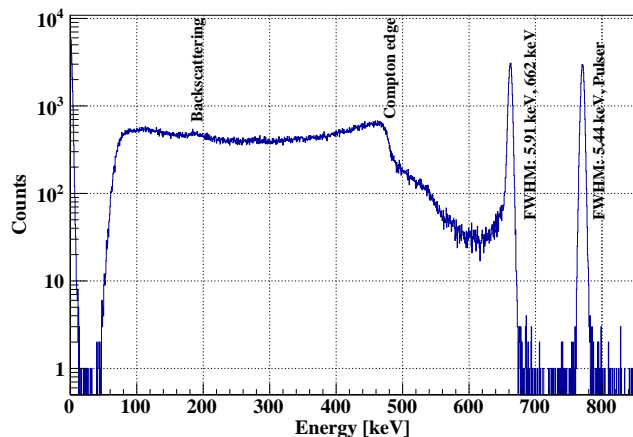


Figure 16 Energy Spectrum of ^{137}Cs taken with detector USD-RL in LAr.

mally after the deployment at MPI. Their leakage current measurement results were shown together with those measured in LN_2 and LAr in Fig. 8, 11, 13 and 15 as references. The energy spectrum of ^{137}Cs taken with detector USD-RL at 1200 V, 78 K in vacuum is shown in Fig. 5.

3 Conclusion and Outlook

The possibility of operating HPGe detectors with thin amorphous germanium contacts directly in LN_2 and LAr has been demonstrated experimentally for the first time. Three detectors with such contacts made at LBNL and USD using USD HPGe crystals survived long-distance transportation, multiple thermal cycles in both cryogenic liquids, and showed reasonable leakage currents and spectroscopic performance. The leakage currents measured for the best detector were under 1 pA at bias voltages well above the depletion voltage. The leakage currents in LAr of the other two detectors were much higher than those measured in LN_2 , mainly due to the side surface leakage.

It has been observed by the GERDA collaboration that the leakage current through the passivated end surfaces of some of their detectors in LAr increased after long-term operation or irradiation with γ -ray sources [39, 40]. It is hence of interest to monitor the leakage current through the side surface of a planar detector passivated with amorphous germanium during long-term operation in LAr. Such measurements will be done with planar detectors with guard contacts at least a year after their fabrication to let their amorphous germanium surfaces stabilize prior to their operation in LAr.

Acknowledgements The authors would like to thank Mark Amman for his instruction on fabricating planar detectors,

and the Nuclear Science Division at Lawrence Berkeley National Laboratory for providing the vacuum cryostat.

References

1. O. Panella, M. Cannoni, C. Carimalo, Y. Srivastava, *Physical Review D* **65**(3), 035005 (2002)
2. F. Almeida Jr, Y. Coutinho, J.M. Simoes, M. Do Vale, *Physical Review D* **62**(7), 075004 (2000)
3. A. Das, N. Okada, D. Raut, *The European Physical Journal C* **78**(9), 696 (2018)
4. W. Rodejohann, *Journal of Physics G: Nuclear and Particle Physics* **28**(6), 1477 (2002)
5. T. Asaka, S. Blanchet, M. Shaposhnikov, *Physics Letters B* **631**(4), 151 (2005)
6. T. Asaka, M. Shaposhnikov, *Physics Letters B* **620**(1-2), 17 (2005)
7. C.S. Fong, E. Nardi, A. Riotto, *Advances in High Energy Physics* **2012** (2012)
8. S. Davidson, A. Ibarra, *Physics Letters B* **535**(1-4), 25 (2002)
9. R. Foot, H. Lew, X.G. He, G.C. Joshi, *Zeitschrift für Physik C Particles and Fields* **44**(3), 441 (1989)
10. R.N. Mohapatra, G. Senjanović, *Physical Review Letters* **44**(14), 912 (1980)
11. Y. Cai, T. Han, T. Li, R. Ruiz, *Frontiers in Physics* **6**, 40 (2018)
12. M.J. Dolinski, A.W. Poon, W. Rodejohann, *Annual Review of Nuclear and Particle Science* **69**, 219 (2019)
13. A. Giuliani, *Acta Phys. Polon.* **41**, 1447 (2010)
14. M. Agostini, A. Bakalyarov, M. Balata, I. Barabanov, L. Baudis, C. Bauer, E. Bellotti, S. Belogurov, A. Bettini, L. Bezrukov, et al., *Physical review letters* **120**(13), 132503 (2018)
15. M. Agostini, A. Bakalyarov, M. Balata, I. Barabanov, L. Baudis, C. Bauer, E. Bellotti, S. Belogurov, S. Belyaev, G. Benato, et al., *The European Physical Journal C* **78**(5), 388 (2018)
16. N. Abgrall, et al., (AIP Publishing, 2017), vol. 1894, p. 020027
17. C. Aalseth, N. Abgrall, E. Aguayo, S. Alvis, M. Amman, I. Arnquist, F. Avignone III, H. Back, A. Barabash, P. Barbeau, et al., *Physical review letters* **120**(13), 132502 (2018)
18. G. Giovanetti, P-type point contact germanium detectors and their application in rare-event searches, Ph.D. thesis, University of North Carolina, (2015)
19. S. Mertens, A. Hegai, D. Radford, N. Abgrall, Y.D. Chan, R. Martin, A. Poon, C. Schmitt, *Nuclear Instruments and Methods in Physics Research Section A: Accelerators, Spectrometers, Detectors and Associated Equipment* **921**, 81 (2019)
20. D. Barrientos, A. Boston, H. Boston, B. Quintana, I. Sagrado, C. Unsworth, S. Moon, J. Cresswell, *Nuclear Instruments and Methods in Physics Research Section A: Accelerators, Spectrometers, Detectors and Associated Equipment* **648**, S228 (2011)
21. M. Agostini, E. Bellotti, R. Brugnera, C. Cattadori, A. D'Andragora, A. Di Vacri, A. Garfagnini, M. Laubenstein, L. Pandola, C. Ur, *Journal of Instrumentation* **6**(04), P04005 (2011)
22. J. Llacer, E. Haller, R. Cordi, *IEEE Transactions on Nuclear Science* **24**(1), 53 (1977)
23. T. Alexander, H.O. Back, W. Bonivento, M. Boulay, P. Collon, Z. Feng, M. Foxe, P.G. Abia, P. Giampa, C. Jackson, et al., arXiv preprint arXiv:1901.10108 (2019)
24. P. Luke, C. Cork, N. Madden, C. Rossington, M. Wesela, *IEEE transactions on nuclear science* **39**(4), 590 (1992)
25. P. Luke, R. Pehl, F. Dilmanian, *IEEE transactions on nuclear science* **41**(4), 976 (1994)
26. P. Luke, M. Amman, B. Philips, W. Johnson, R. Kroeger, *IEEE Transactions on Nuclear Science* **47**(4), 1360 (2000)
27. M.S. Amman, P.N. Luke, in *Hard X-Ray, Gamma-Ray, and Neutron Detector Physics II*, vol. 4141 (International Society for Optics and Photonics, 2000), vol. 4141, pp. 144–156
28. W.L. Hansen, E.E. Haller, *IEEE Transactions on Nuclear Science* **24**(1), 61 (1977)
29. M. Amman, arXiv preprint arXiv:1809.03046 (2018)
30. J.L. Chiu, S. Boggs, H.K. Chang, J. Tomsick, A. Zoglauer, M. Amman, Y.H. Chang, Y. Chou, P. Jean, C. Kierans, et al., *Nuclear Instruments and Methods in Physics Research Section A: Accelerators, Spectrometers, Detectors and Associated Equipment* **784**, 359 (2015)
31. C.A. Kierans, S.E. Boggs, J.L. Chiu, A. Lowell, C. Sleator, J.A. Tomsick, A. Zoglauer, M. Amman, H.K. Chang, C.H. Tseng, et al., arXiv preprint arXiv:1701.05558 (2017)
32. X.H. Meng, G.J. Wang, M.D. Wagner, H. Mei, W.Z. Wei, J. Liu, G. Yang, D.M. Mei, *Journal of Instrumentation* **14**(02), P02019 (2019)
33. W.Z. Wei, X.H. Meng, Y.Y. Li, J. Liu, G.J. Wang, H. Mei, G. Yang, D.M. Mei, C. Zhang, *Journal of Instrumentation* **13**(12), P12026 (2018)
34. I. Abt, A. Caldwell, D. Lenz, J. Janicsko, J. Liu, X. Liu, B. Majorovits, F. Stelzer, *J. Phys. Conf. Series* **203**(1), 012135 (2010)

35. E. Hull, R. Pehl, Nucl. Instr. and Meth. A **538** (2005)
36. Q. Looker, M. Amman, K. Vetter, Nuclear Instruments and Methods in Physics Research Section A: Accelerators, Spectrometers, Detectors and Associated Equipment **777**, 138 (2015)
37. W.Z. Wei, R. Panth, J. Liu, H. Mei, D.M. Mei, G.J. Wang, The Impact of the Charge Barrier Height on Germanium (Ge) Detectors with Amorphous-Ge Contacts for Light Dark Matter Searches (2020). ArXiv: 2002.04462
38. D.M. Mei, R. Mukund, W.Z. Wei, R. Panth, J. Liu, H. Mei, Y.Y. Li, P. Acharya, S. Bhattarai, K. Kooi, et al., arXiv preprint arXiv:1909.05806 (2019)
39. M.B. Heider, C. Cattadori, O. Chkvorets, A. Di Vacri, K. Gusev, S. Schonert, M. Shirchenko, in *2008 IEEE Nuclear Science Symposium Conference Record* (IEEE, 2008), pp. 3513–3516
40. D. Palioselitis, G. collaboration, et al., in *Journal of Physics: Conference Series*, vol. 606 (IOP Publishing, 2015), vol. 606, p. 012007